JOURNAL OF GEOPHYSICAL RESEARCH, VOL. 113, B03403, doi:10.1029/2007JB005063, 2008

Space geodetic investigation of the coseismic and postseismic deformation due to the 2003 M_w7.2 Altai earthquake: Implications for the local lithospheric rheology

Sylvain Barbot,[1] Yariv Hamiel,[1,2] and Yuri Fialko[1]

Received 21 March 2007; revised 21 September 2007; accepted 25 October 2007; published 12 March 2008.

[1] We use Envisat Advanced Synthetic Aperture Radar data and SPOT optical imagery to investigate the coseismic and postseismic deformation due to the 27 September 2003, M_w7.2 Altai earthquake, which occurred in the Chuya Basin near the Russia-China-Mongolia border. On the basis of the synthetic aperture radar (SAR) and SPOT data, we determined the rupture location and developed a coseismic slip model for the Altai earthquake. The inferred rupture location is in a good agreement with field observations, and the geodetic moment from our slip model is consistent with the seismic moment determined from the teleseismic data. While the epicentral area of the Altai earthquake is not optimal for radar interferometry (in particular, due to temporal decorrelation), we were able to detect a transient signal over a time period of 3 years following the earthquake. The signal is robust in that it allows us to discriminate among several commonly assumed mechanisms of postseismic relaxation. We find that the postearthquake interferometric SAR data do not warrant poroelastic rebound in the upper crust. The observed deformation also disagrees with linear viscoelastic relaxation in the upper mantle or lower crust, giving rise to a lower bound on the dynamic viscosity of the lower crust of the order of 10^{19} Pa s. The data can be explained in terms of fault slip within the seismogenic zone, on the periphery of areas with high coseismic slip. Most of the postseismic deformation can be explained in terms of seismic moment release in aftershocks; some shallow slip may have also occurred aseismically. Therefore the observed postseismic deformation due to the Altai earthquake is qualitatively different from deformation due to other similarly sized earthquakes, in particular, the Landers and Hector Mine earthquakes in the Mojave desert, southern California. The observed variations in the deformation pattern may be indicative of different rheologic structure of the continental lithosphere in different tectonically active areas.

Citation: Barbot, S., Y. Hamiel, and Y. Fialko (2008), Space geodetic investigation of the coseismic and postseismic deformation due to the 2003 M_w7.2 Altai earthquake: Implications for the local lithospheric rheology, *J. Geophys. Res.*, *113*, B03403, doi:10.1029/2007JB005063.

1. Introduction

[2] On 27 September 2003, a M_w7.2 right-lateral strike-slip earthquake occurred in the Chuya Basin in the mountainous Altai region, near the Russia-China-Mongolia border (Figure 1). In the following few days, the Altai earthquake generated a robust sequence of aftershocks with moment magnitudes up to M_w6.6 [*Ekström et al.*, 2005; *Nissen et al.*, 2007]. The M_w7.2 main shock is the largest earthquake in 70 years to occur in the Altai range, since the right-lateral strike-slip M_w7.9 Fu-Yun earthquake which struck the northeastern Junggar basin in 1931.

[3] The Altai intraplate mountain ranges stretch from southwestern Siberia to the Gobi desert over a length of 1700 km. The tectonically active Altai ranges formed in the late Cenozoic in response to a northeast compression coming from the India-Eurasia collision 2000 km to the south [*Tapponier and Molnar*, 1979] and to a radial extension due to the warm, buoyant Hangay Dome area in central Mongolia to the east [*Cunningham*, 1998]. The Altai region is kinematically separate from the Hangay Dome, with a colder lithosphere and a greater elastic thickness [*Windley and Allen*, 1993; *Bayasgalan et al.*, 2005]. The Altai orogen includes two distinct mountain belts: the right-lateral transpressive western (or Mongolian) Altai and the left-lateral transpressive Gobi Altai. The western Altai is dominated by a regional N-S shortening and N-NW trending right-lateral strike-slip faults that terminate in NW trending thrust faults [*Cunningham*, 2005]. In the Gobi Altai domain, these stresses are accommodated by transpressive, E-W, left-lateral strike-slip faults with interseismic slip rates of the

[1]Institute of Geophysics and Planetary Physics, Scripps Institution of Oceanography, University of California, San Diego, La Jolla, California, USA.
[2]Now at the Geological Survey of Israel, Jerusalem, Israel.

0148-0227/08/2007JB005063$09.00

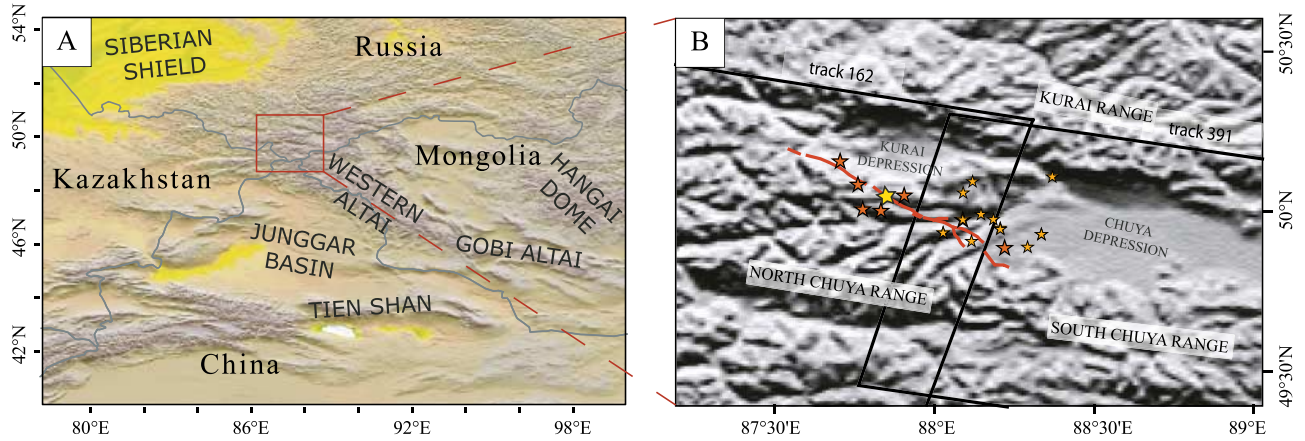

Figure 1. Location of the 27 September 2003, M_w7.2 Altai earthquake, near the Russia-China-Mongolia border. (a) Major geologic structures on the regional scale. (b) Location of the epicenter (yellow star), with the following days $M_w \geq 6$ aftershocks (red stars). The black frames indicate the radar swath of Envisat tracks 434 and 391. Orange stars indicate aftershocks of M_w5 and above after 22 December 2003.

order of 1 mm/a, as constrained by GPS observations [*Calais et al.*, 2003].

[4] Large earthquakes are usually followed by transient surface deformation with velocities that exceed those for interseismic deformation. Such deformation transients present an opportunity to improve our understanding of the physical processes involved in crustal and upper mantle deformation. The instantaneous deformation field accompanying an earthquake can be explained assuming linear elastic deformation of the ambient rocks [*Fialko*, 2004a; *Fialko et al.*, 2005]. Transient strains are systematically observed in years to decades following large earthquakes [*Stein and Lisowski*, 1983; *Reilinger*, 1986; *Thatcher*, 1983; *Kenner and Segall*, 2000], yet there is no consensus regarding constitutive laws that govern the mechanical time-dependent processes in the postseismic epoch.

[5] One mechanism often invoked to explain postseismic transients is afterslip on the ruptured fault or its extension. Evidence for afterslip is provided by kinematic inversions of geodetic data [*Savage et al.*, 1994; *Fialko*, 2004b; *Freed et al.*, 2006], although different physical explanations can be invoked to describe the process dynamics [*Tse and Rice*, 1986; *Dieterich*, 1987; *Fialko*, 2004b; *Perfettini and Avouac*, 2004]. Another commonly considered mechanism is the aseismic viscoelastic relaxation in the lower crust and upper mantle. The possibly ductile lower crust and upper mantle might not be able to sustain increases in deviatoric stresses due to the main shock. The coseismically induced change in the deviatoric stress below the brittle-ductile transition might be relieved by viscous flow [*Nur and Mavko*, 1974; *Pollitz*, 1997; *Deng et al.*, 1999]. If the viscous deformation is involved in postseismic transients, observations indicate that simple linear viscoelastic models are inadequate. In particular, the latter fail to explain the temporal and spatial characteristics of deformation transients following the Mojave desert earthquakes, suggesting that multiple relaxation times and/or stress-dependent viscosities may be necessary [*Pollitz*, 2003; *Fialko*, 2004b; *Freed and Bürgmann*, 2004]. Third suggested mechanism is the poroelastic rebound of the upper crust [*Reid*, 1910]. For example, the postseismic transient following the 1992 Landers earthquake has been explained by a combination of poroelasticity above the brittle-ductile transition and a localized shear on the deep part of the fault [*Peltzer et al.*, 1998; *Fialko*, 2004b]. Probably the best documented example of poroelastic rebound is the one that occurred in the first few months following two June 2000 earthquakes in south Iceland: [*Jónsson et al.*, 2003] demonstrated that both surface deformation and water level changes in geothermal wells are consistent with the pore pressure diffusion in response to the coseismic stress changes.

[6] In this study, we compare the predictions of each candidate mechanism to a set of interferometric data covering 3 years of postseismic deformation following the 2003 Altai earthquake. In section 2, we describe the coseismic rupture, as constrained by synthetic aperture radar (SAR) amplitude cross correlation, azimuthal interferometry and SPOT optical image cross correlation. In section 3, we present the interferometric data characterizing the postseismic deformation and compare them to predictions of the afterslip, viscoelastic and poroelastic models. Finally, we discuss the implications from these results for the mechanical properties of the Altai lithosphere and variations in rheology among different tectonically active environments.

2. Coseismic Analysis

2.1. Determination of the Fault Location

[7] The Altai earthquake struck the northern part of the western Altai. The 70 km long rupture cut through the Chuya Range immediately SW of the Kurai and Chuya depressions [*Nissen et al.*, 2007]. Because of the remote location of the earthquake, few ground-based observations are available. We investigated the earthquake rupture using space geodetic data. The coseismic deformation was captured by several independent Envisat SAR pairs. Figure 2 shows interferograms from Envisat track 391, spanning a time interval between 8 September 2003 and 13 October

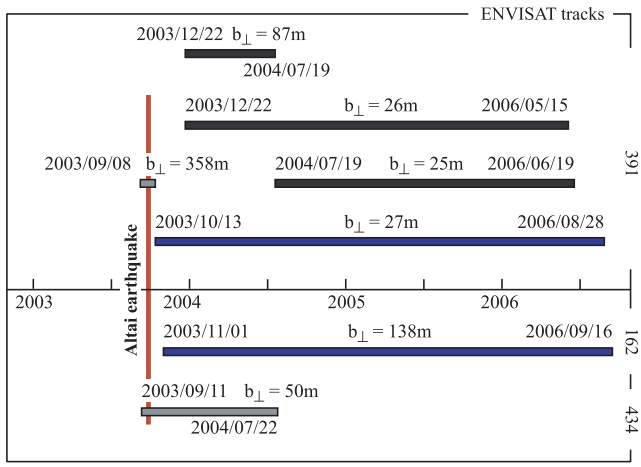

Figure 2. Coseismic and postseismic interferograms used in this study. The (grey) coseismic interferograms were jointly used to invert for the coseismic slip on the fault. The 3 year (blue) pairs were simultaneously inverted for afterslip. Other (black) pairs are used to verify the early stage of the postseismic transient approximatively 6 months, 2 years, and 2.5 years after the Altai earthquake.

2003, and from track 434, spanning a time interval between 11 September 2003 and 22 July 2004. Unfortunately, the interferometric SAR (InSAR) coherence is poor in the near field and to the south of the rupture due to temporal decorrelation [*Zebker and Villasenor*, 1992] in the Chuya Range, so we could not use the radar line-of-sight phase information to determine the fault location. We found along-track InSAR data [*Bechor and Zebker*, 2006] to be more useful for this purpose, the along-track interferometry being less sensitive to temporal decorrelation. The along-track interferogram exploits a parallax effect to detect the surface displacement in the azimuthal (along-track) direction. The along-track interferometry is a high-resolution phase measurement equivalent to the azimuthal offsets [*Michel et al.*, 1999; *Peltzer et al.*, 1999; *Fialko et al.*, 2001]. The details of our implementation of the along-track interferometry are given in Appendix A. We processed the raw SAR data using the ROI_PAC software [*Rosen et al.*, 2000] that was modified to compute the along-track interferograms. In our experience, successful along-track interferometry requires baselines that are a factor of two smaller than those required for the conventional radar line-of-sight (LOS) interferometry. Given the relatively large baselines of the coseismic SAR data for Altai, the along-track interferogram is affected by the baseline decorrelation. A displacement contrast is visible across the fault, but the measurement is complicated by the WNW-ESE fault orientation, almost normal to the satellite track. The range offset data are less sensitive to changes in the reflective properties of the ground compared to the radar phase (LOS) data, and therefore provide useful information on displacements near the fault trace (Figures 3c and 3d), given the favorable fault orientation along the radar range. We also analyzed SPOT5 panchromatic optical images [*Van Puymbroeck et al.*, 2000]. We used the cross-correlation software COSI-Corr [*Leprince et al.*, 2007] to compute the deformation that occurred between two acquisitions bracketing the earthquake (9 September 2003 to 17 January 2004, frame K215-J249). This approach allows one to measure horizontal displacements with an accuracy up to 5 cm, in the E-W and N-S directions. The inferred signal in the E-W displacement component reveals a discontinuity consistent with the right-lateral strike-slip motion (Figure 3a). The N-S component of the SPOT cross correlation shows no significant displacement contrast across the fault and is not shown here. The SPOT data alone do not provide a precise fault location presumably due to temporal decorrelation and nonoptimal orbital baseline.

[8] Our simplified fault geometry (see thick black line in Figure 3) consists of six rectangular segments, rotating from an almost NE-SW strike in the westernmost section to a NNE-SSW strike in the middle section, west of the Chuya depression. We also identified a short SW-NE striking segment at the southern tip of the rupture based on the SAR offset data. The latter segment probably corresponds to a M_w6.6 subevent that occurred several hours after the main shock near the Chuya basin. Our estimation of the fault location, based on space geodetic data, agrees well with the field mapping of *Nissen et al.* [2007] (red profile in Figure 3).

2.2. Inversion for Coseismic Model

[9] The coseismic slip model plays an important role in studies of postseismic relaxation as it provides the initial condition exciting the time-dependent response of the lithosphere. Observed coseismic deformation can often be explained by simple models based on solutions for dislocations in an elastic half-space [*Massonnet et al.*, 1993; *Fialko et al.*, 2001, 2005; *Hamiel and Fialko*, 2007]. Solutions for surface displacements due to dislocations in elastic half-space are readily available for both homogeneous [*Okada*, 1985] and layered media [*Wang et al.*, 2003]. As the velocity structure of the Earth's crust in the western Altai area is poorly known, we assume a homogeneous half-space with a Poisson's ratio of $\nu = 0.25$. Previous work has shown that reasonable variations in the elastic moduli with depth have only moderate effect on the inferred slip models [*Zhu and Rivera*, 2002; *Simons et al.*, 2002; *Fialko*, 2004a; *Hamiel and Fialko*, 2007].

[10] Our slip model for the Altai earthquake was obtained from the inversion of SAR line-of-sight data, using a three-dimensional elastic half-space solution [*Okada*, 1985]. We extended the six segments down to a depth of 21 km and discretized each segment into 2×3 km patches in the strike and dip direction respectively. Each individual patch is allowed to slip in the strike and dip directions. The inversion for slip on the fault involves a regularized least squares optimization. The residuals between the computed surface displacements, projected onto the LOS direction, and the measured SAR LOS displacements are minimized through an iterative procedure. The added regularization constraint is covariance between neighboring fault elements and no slip at the bottom and sides of the fault. Details on the data reduction and the inversion procedure are given by *Fialko* [2004a]. We inverted simultaneously the Envisat pairs 8 September 2003 to 13 October 2003, track 391 and 11 September 2003 to 22 July 2004, track 434 (Figure 4) because the fault extends across multiple satellite tracks.

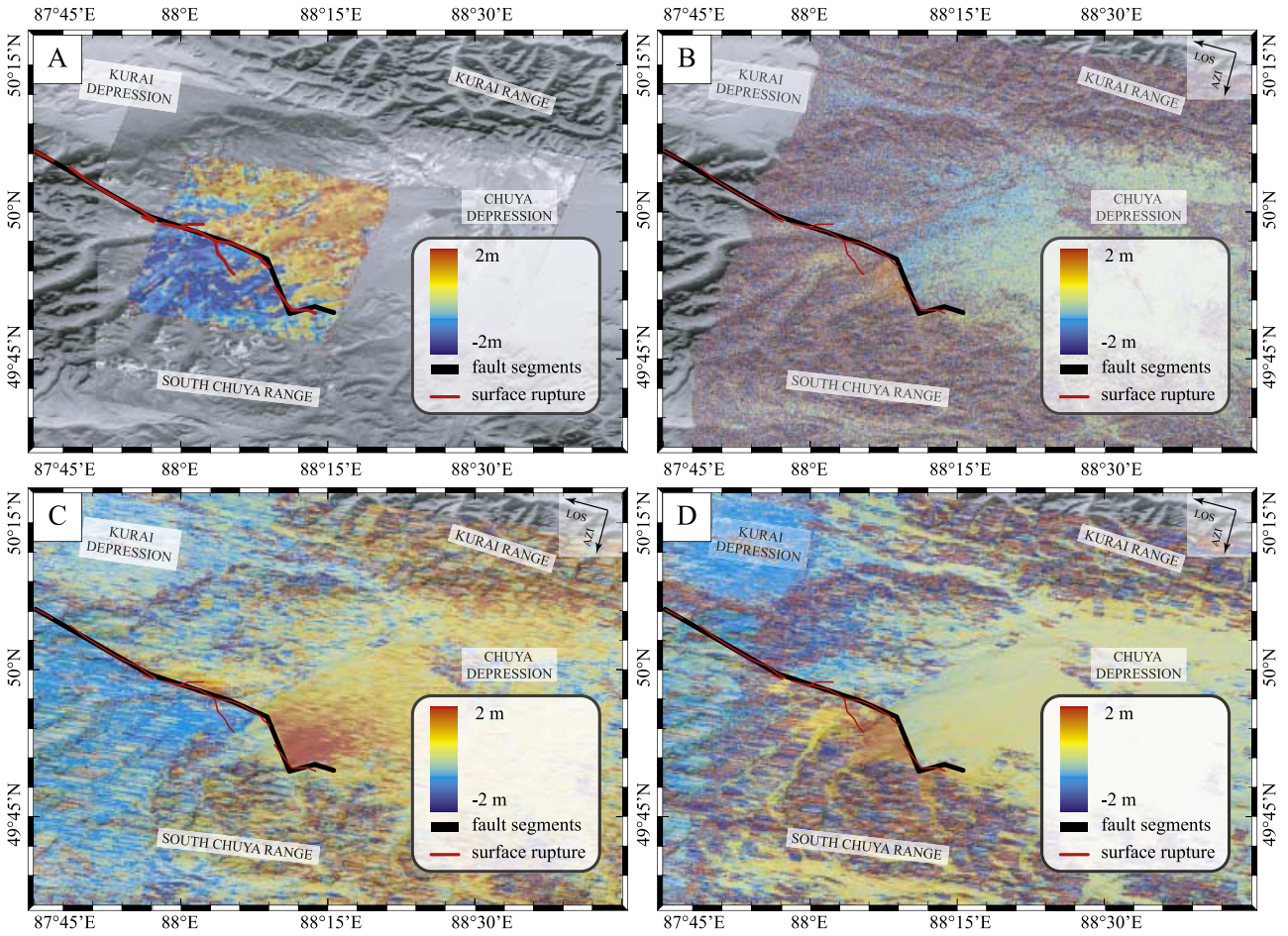

Figure 3. Coseismic data analysis and fault location. (a) East component of the SPOT correlation which reveals a clear right-lateral motion across the fault. The SPOT optical data are overlaid on the topography. (b) Fine resolution of the along-track interferogram (8 September 2003 to 13 October 2003, track 391) showing where the fault ruptured. (c) Range offsets of pairs 8 September 2003 to 13 October 2003, track 391, and 11 September 2003 to 22 July 2004, track 434, revealing two apparently separated dextral ruptures. (d) Azimuthal offset of interferogram 8 September 2003 to 13 October 2003. The color scale has been saturated to highlight the fault location. The thick black line in each image is our estimate of the fault location. The thin red line is the survey of *Nissen et al.* [2007]. The AZI and LOS arrows indicate the satellite orbital direction (15°) and the look direction, with a 23° incidence. Positive LOS displacements are toward the satellite.

The inclusion of track 434 data was needed to constrain slip on the western part of the fault. There are some discrepancies between the estimated focal mechanisms of the main shock and the first large aftershocks. The 27 September 2003 main shock was a subvertical right-lateral event which dip angle was estimated between 71° [*Ekström et al.*, 2005] and 82° [*Nissen et al.*, 2007]. We estimated the dip angle of each segment by performing a grid search between 60° and 120° and identifying the smallest misfit with the SAR LOS observations. We found that quite different dip angles along the fault gave rise to similar misfits. As the coherence is poor in the near field and south of the fault (Figure 4), the InSAR LOS data alone are not sufficient to constrain the fault dip angle. We performed a similar grid search for the best fitting dip angle for each segment, inverting pixel tracking data (range and azimuthal offsets), which are less affected by decorrelation near the fault trace. The best fitting model gave rise to segment orientation of less than 5° from the vertical. Inversions of InSAR phase and pixel offsets (both individually and jointly) gave rise to systematic residuals in the azimuthal offsets near the fault kink. We attempted to constrain the dip angles required by the azimuthal InSAR data. The required dip angles for each segment were also subvertical but oriented to the south, that is, opposite to those inferred from range offsets or phase change. As the vertical fault model was within the family of models giving the best variance reduction, we assumed that all fault segments are vertical (Figure 4c). The residuals from range offsets (Figure 4e) reveal a zone of deformation to the south of the rupture that cannot be explained by slip on the fault plane as residuals appear on both sides of the fault. Azimuth offsets exhibit some asymmetry across the fault, which might be indicative of either dipping rupture, or deviations from the assumption of a laterally homogeneous elastic half-space.

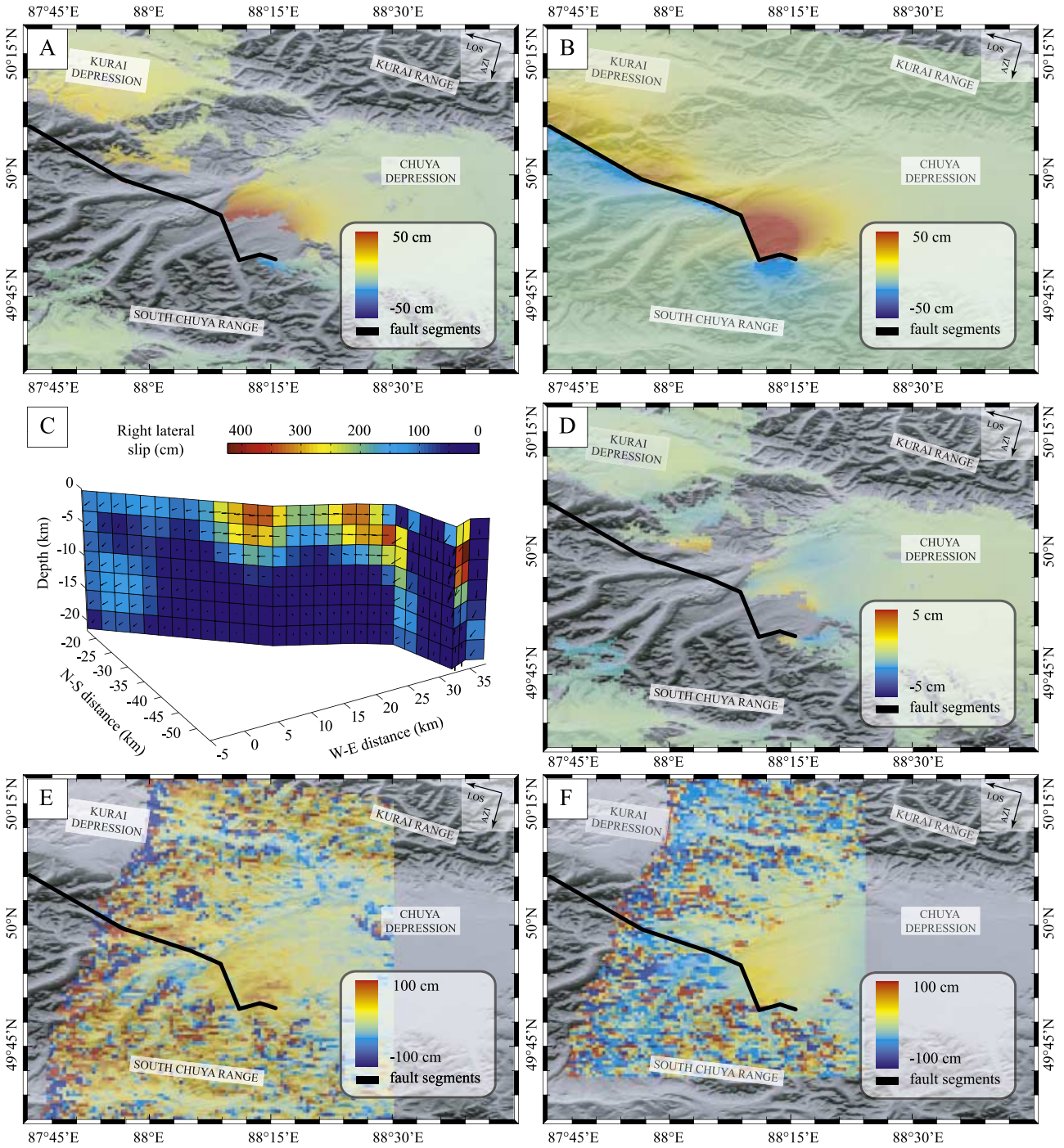

Figure 4. Coseismic slip inversion. (a) Interferograms (8 September 2003 to 13 October 2003, track 391, and 11 September 2003 to 22 July 2004, track 434) used to invert for a coseismic slip model. (b) Model coseismic LOS displacements. (c) Coseismic slip distribution obtained after inversion of LOS displacements of the 2 interferograms in Figure 4a. The black arrows indicate the direction and amplitude of slip for every patch. (d) LOS displacement residuals after inversion. (e) Range offset residuals. (f) Azimuthal offset residuals.

[11] The coseismic slip model shows three patches of relatively high slip, which correspond to the main rupture and the immediate large aftershocks. The second segment from the eastern end of the rupture has a total seismic moment of M_w = 6.7, which agrees with the moment magnitude of a thrusting event that occurred several hours after the earthquake as estimated by *Ekström et al.* [2005]. This aftershock is located at the edge of the Chuya basin, in agreement with the relocation of *Nissen et al.* [2007]. According to our slip model, the maximum surface offsets are less than 4 m. Most of the slip occurs at relatively shallow depths, from the surface to about 9 km depth. The

western section of the fault slip model shows about 1 m slip at greater depth, but is relatively poorly constrained by the SAR data. According to our slip model the total seismic moment is $M_0 = 4.8 \times 10^{19}$ N m (corresponding to a moment magnitude $M_w = 7.1$), in fair agreement with the estimated moment derived from broadband teleseismic data $M_w = 7.2$ [*Ekström et al.*, 2005]. It should be noted that we invert for the total slip that occurred coseismically and during the first 16 d following the main shock. The corresponding forward model (Figure 4b), projected onto the LOS direction (positive toward the satellite), is qualitatively consistent with the coseismic model of *Nissen et al.* [2007].

3. Postseismic Deformation

3.1. Inversion for Afterslip Model

[12] We used SAR LOS interferometry to look at the postseismic transients. We processed the available Envisat data from tracks 391 and 162 (Figure 2) and identified the LOS displacements common to all interferograms within the 3 year transient following the earthquake. The postseismic interferograms clearly show strain accumulation at the southern tip of the fault, in the Chuya basin (Figure 5). The positive LOS displacements at the southern tip of the rupture are not due to tropospheric noise [*Tarayre and Massonnet*, 1996], as the signal appears in four independent interferograms. The observed postseismic signal is localized close to the fault, with wavelengths much smaller than the fault length but of the order of the fault locking depth (5–10 km). Note that the near-field LOS postseismic displacements have the same sign as the coseismic ones.

[13] The wavelength of the postseismic transient and the polarity of the LOS displacements appear to favor a shallow slip on the earthquake rupture. We carried out a kinematic inversion for the postseismic slip using two 3 year interferograms (13 October 2003 to 28 August 2006, track 391 and 1 November 2003 to 16 September 2006, track 162). As the 3 year interferograms have a somewhat different spatial coverage, we performed a joint inversion, simultaneously minimizing the residuals between both interferograms and our model. The joint inversion allows us to reduce the tropospheric contribution of each interferogram. We used the same homogenous half-space model and fault model as in the coseismic inversion. We initially performed the inversion allowing for slip on a deeper extension of the fault but such an inversion did not require any slip at depth greater than 21 km. Consequently, we chose a fault geometry that is the same as the coseismic one in order to facilitate the model comparison (Figure 5c). In our best fitting model, most of the postseismic slip occurs in the seismogenic zone, mainly above 6 km depth. The slip amplitude and depth of the inferred slip model are robust to perturbations in dip angles, as verified by inversions with variable dip angles on each segment, due to the short wavelength of the surface deformation. The maximum slip occurred on the third segment from the eastern end of the fault, in the middle of two relatively high coseismic slip patches. The residuals of the inversion (Figures 5e–5f) are concentrated in the North Chuya Range, in the middle section of the fault trace. Apart from these localized residuals, the bulk of the postseismic SAR data is well explained by the afterslip model. This suggests that most of the postseismic LOS displacements may represent slip (seismic or aseismic) on parts of the fault in the nominal seismogenic depth interval.

3.2. Poroelastic Rebound

[14] The occurrence of a large earthquake alters the pore pressure in the crust close to the rupture. The induced volumetric strain can create significant pore pressure gradients that are relaxed by the movement of fluids following favorably the paths of maximum permeability in the host rocks. The coupling between the pore fluid diffusion and the effective elastic properties introduces a time dependence into the response of the solid matrix [*Reid*, 1910; *Biot*, 1941; *Coussy*, 2004]. Fluids are usually assumed to be pervasive in the Earth's crust, so the poroelastic rebound is a likely physical mechanism contributing to the postseismic deformation. On the basis of theoretical arguments, pore fluid diffusion should occur at intermediate wavelengths from near field to about 2.5 fault lengths from the fault [*Piombo et al.*, 2005], and the coseismic stress changes should be significantly altered on a timescale controlled by the hydraulic diffusion. The pore pressure readjustment was estimated to be several years long in case of the Landers earthquake [*Peltzer et al.*, 1998; *Fialko*, 2004b], but only a few months long in case of the 2000 south Iceland earthquakes [*Jónsson et al.*, 2003]. Radar interferometry is highly sensitive to the vertical component of the deformation field and is therefore well suited to detect poroelastic rebound [e.g., *Peltzer et al.*, 1998]. As the pore pressure dissipates, owing to the fluid diffusion, there is a gradual change of Poisson's ratio in the crustal rocks from the undrained conditions immediately after the earthquake to the lower, drained, values [*Peltzer et al.*, 1998; *Biot*, 1941; *Coussy*, 2004]. We compute surface displacements corresponding to complete fluid diffusion by choosing the average value of the drained Poisson's ratio $\nu_d = 0.20$. The prediction of the postseismic transient (the difference between the drained and undrained states), projected in the LOS direction, is shown in Figure 6. The poroelastic rebound model agrees relatively well with the 13 October 2003 to 28 August 2006 interferogram (Figure 5a) in the North Chuya Range, in the south side of the fault's midsection. At this location, however, the afterslip model and the poroelastic model predict the same polarity of line-of-sight displacements. The LOS displacement in the South Chuya Range and the Chuya Basin, where both InSAR observations are consistent, is essentially opposite to the poroelastic model (Figures 5a and 5b). The poroelastic rebound of the upper crust therefore cannot explain the InSAR data. Analysis of interferograms spanning 1 year of postseismic deformation showed that the surface displacements had the same polarity during the observation period, suggesting that no significant poroelastic rebound occurred in the 3 years following the Altai earthquake.

3.3. Viscoelastic Relaxation

[15] We also investigated a possibility of a viscoelastic response of the Altai lithosphere. The viscoelastic relaxation can explain a variety of observations from laboratory experiments [e.g., *Karato and Wu*, 1993] to large-scale lithospheric rebounds [*Thatcher and Rundle*, 1979; *Peltier*,

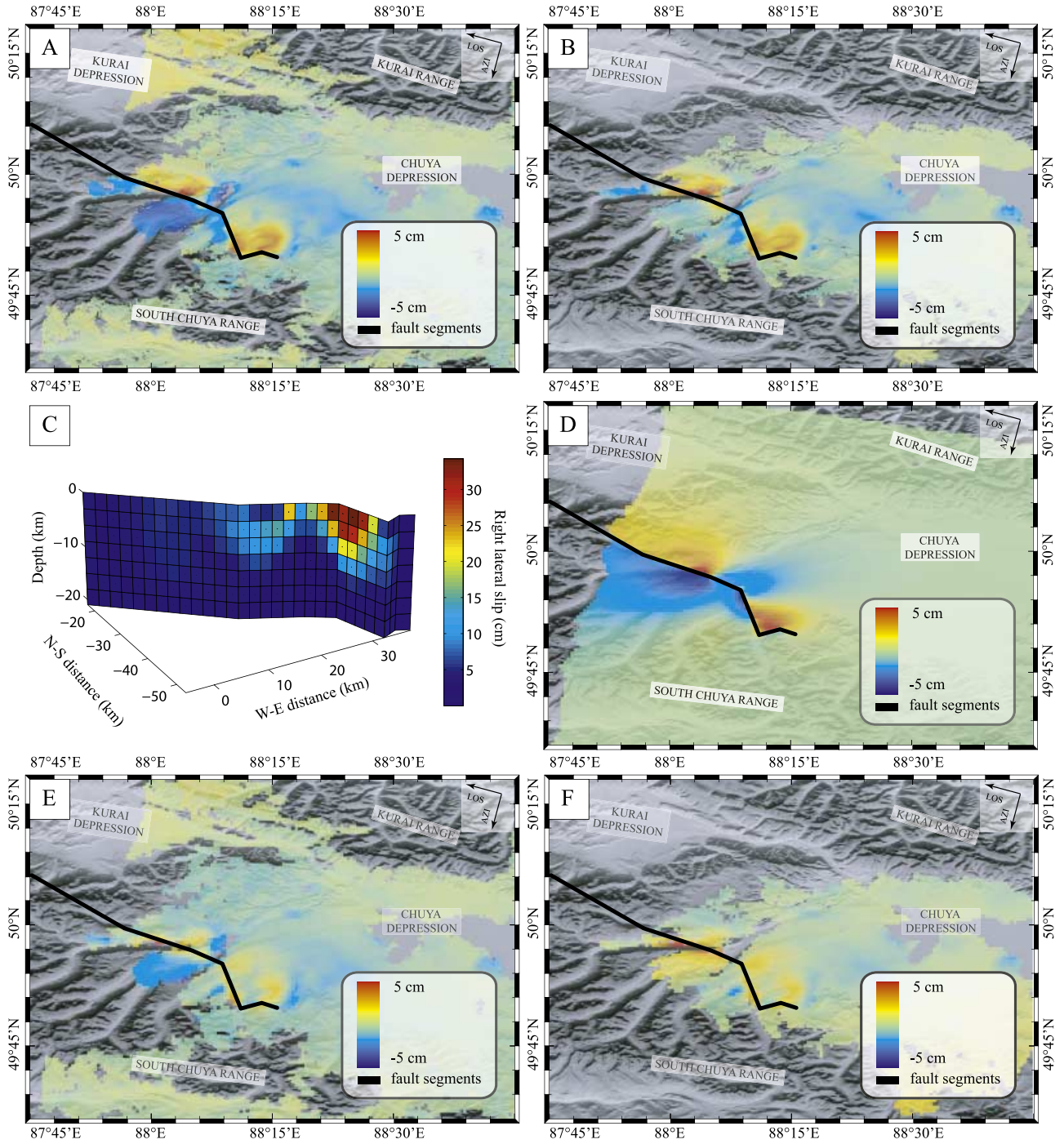

Figure 5. Postseismic interferograms and inversion for the afterslip model. (a) Interferogram 13 October 2003 to 28 August 2006, track 391, showing 3 years of postseismic deformation, projected in the LOS direction. (b) Interferogram 1 November 2003 to 16 September 2006, track 162, showing also 3 years of postseismic deformation. (c) Afterslip model showing a slip distribution confined in the seismogenic zone. (d) Forward model, fitting the two 3 year interferograms. (e–f) Residuals on interferograms in Figures 5a and 5b, respectively.

1981]. High-temperature, high-pressure creep experiments suggest that the effective viscosity is controlled by the thermal properties of the lithosphere and the stress to which it is subjected [e.g., *Larsen et al.*, 1996; *Gasperini et al.*, 2004]. A higher geotherm implies a weaker lower crust and a faster viscous relaxation. A direct way of characterizing properties of the ductile substrate is to infer its viscosity structure from the transient response to the coseismic excitation. Little is known about the effective rheology of the lower crust and upper mantle in the Altai area. Previous studies in other tectonic environments have considered Maxwellian materials [*Pollitz et al.*, 2000; *Fialko*, 2004b; *Freed et al.*, 2006], standard linear solids [*Pollitz et al.*, 2000], bilinear solids [*Pollitz*, 2003] and nonlinear power

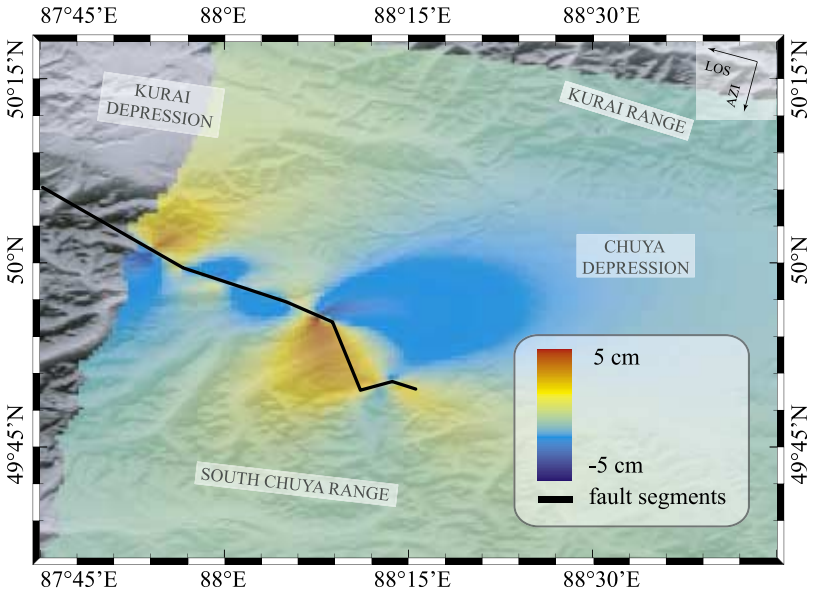

Figure 6. Predictions of the full poroelastic rebound following Altai earthquake. The model is obtained by differentiating the two elastic responses of the crust with an undrained Poisson's ratio $\nu_u = 0.25$ and with a drained Poisson's ratio $\nu_d = 0.20$.

law rheologies [*Freed and Bürgmann*, 2004]. As we have little information on the structure of the lithosphere in the Mongolian Altai, we used a simplified, vertically stratified model with a Maxwellian viscoelastic body. We have tested three end-member rheologic models, having a different shear viscosity structure, all elastic parameters being otherwise the same (Table 1). All models have in common an elastic upper crust down to a depth of 15 km. Variations in the rheologic structure give rise to distinct wavelengths and timescales in the time-dependent response at the Earth's surface. We performed simulations of the viscoelastic relaxation due to the Altai earthquake using the approach developed by *Wang et al.* [2006] for a layered viscoelastic Earth model in the presence of gravity. In these simulations, we used our coseismic slip model (Figure 4c) and the rheologic parameters shown in Table 1.

[16] We computed the entire time series of the postseismic transient and then simulated the SAR data (13 October 2003 to 28 August 2006) by computing the difference between the surface deformation corresponding to the SAR acquisition dates, projected onto the satellite LOS. The resulting surface displacements are shown in Figure 7. The jelly sandwich model [*Brace and Kohlstedt*, 1980] and the weak lower crust model produce very similar results for any value of the upper mantle viscosity in the range $\eta = 10^{18}-10^{25}$ Pa s. This indicates that the postseismic deformation we observe at the surface is not sensitive to variations in rheology at depths greater than 35 km (about four fault depths). The weak lower crust rheology yields a deformation with wavelengths comparable to the thickness of the elastic upper crust, whereas the weak mantle rheology gives a surface deformation with a larger wavelength, of the order of the Moho depth. This illustrates the self-similar behavior of the solution with a wavelength depending upon the relaxation depth and the deformation magnitude controlled by the length of the earthquake. None of the viscoelastic simulations show a strain accumulation as close to the fault as seen in the SAR data. The SAR observations therefore appear to rule out the viscous relaxation as a significant contributor to the postseismic transient on the timescale of 3 years at depths shallower than 35 km.

4. Discussion

[17] The 3 year postseismic transient following Altai earthquake shows a localized deformation at the southernmost part of the fault, in the Chuya basin. This deformation is not consistent with the viscoelastic relaxation in the lower crust or upper mantle as the predicted deformation would have a larger wavelength (Figure 7). In the weak lower crust

Table 1. Viscoelastic Coefficients[a]

	Elastic Moduli		Weak Mantle		Weak Lower Crust		Jelly Sandwich	
	μ, GPa	ν	η, Pa s	τ_m, years	η, Pa s	τ_m, years	η, Pa s	τ_m, years
UC[b]	28	0.28						
LC	45	0.26	1×10^{21}	350	2×10^{18}	0.7	2×10^{18}	0.7
UM	69	0.28	2×10^{18}	0.7	1×10^{18}	0.3	1×10^{25}	3×10^{6}

[a]The parameters are η, viscosity; μ, shear modulus; ν, Poisson's ratio; and τ_m, Maxwell relaxation time. The upper crust (UC) extends from the surface to 15 km; the lower crust (LC) extends from 15 km to the upper mantle (UM) at 35 km.
[b]For the upper crust, the weak mantle, weak lower crust, and jelly sandwich are elastic.

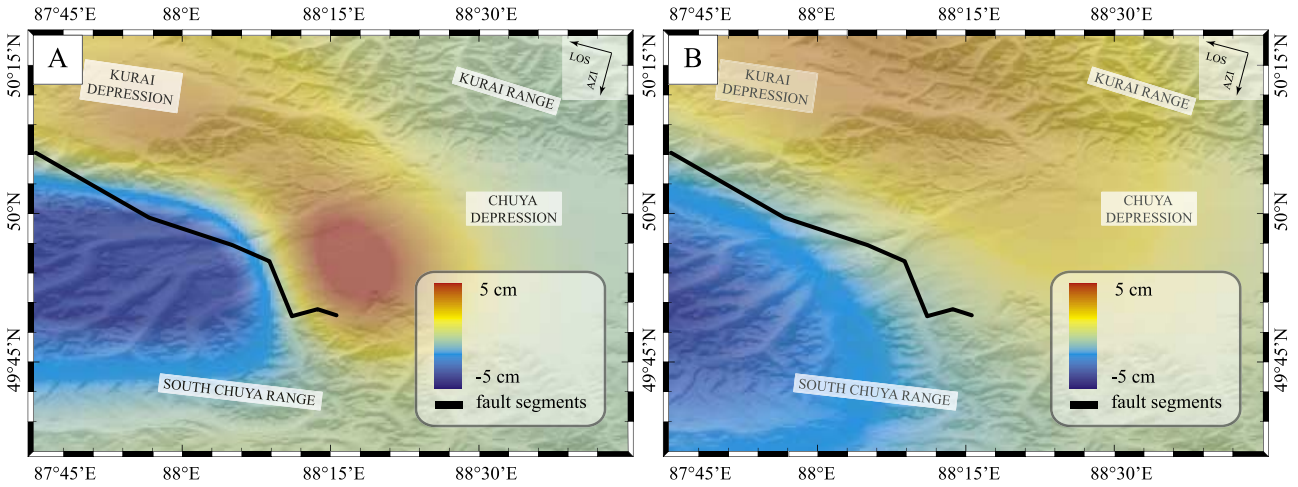

Figure 7. Simulated LOS displacement for 3 years of viscoelastic relaxation occurring between 13 October 2003 and 28 August 2006. (a) Weak lower crust or jelly sandwich rheology. (b) Deformation due to a flow in a weak mantle. Note the larger wavelength of the deformation.

model, the surface deformation is not sensitive to the value of the shear viscosity in the upper mantle, provided that the latter has a relaxation time greater than a few years. These results are consistent with our expectation that the bulk of the surface deformation is controlled by the most inviscid layer. The available data do not have the spatial and temporal coverage to constrain deep viscous flow that might occur in the upper mantle. However, any rapid viscous flow in the lower crust would yield a deformation field with a wavelength well within the detection limit of our SAR images. Therefore we can put a lower bound on the effective shear viscosity of the lower crust in the western Altai of $\eta \geq 10^{19}$ Pa s. This result is consistent with other estimates of the thickness of the brittle layer. The strength of the lithosphere, as constrained by gravity measurements in the western Altai, is believed to reside in the seismogenic layer, which spans the entire crust [*Bayasgalan et al.*, 2005]. Measurements of heat flux were interpreted as indicating that the effective thickness of the lithosphere in the Mongolian Altai is 55 km [*Windley and Allen*, 1993]. While the shallow location of the seismic rupture may not be able to excite significant viscoelastic response in the deep ductile substrate, a longer period of observations of the postseismic deformation might nevertheless better constrain the viscoelastic properties of the lower crust.

[18] The polarity of the LOS displacement shows that the poroelastic rebound of the upper crust cannot explain the observed transient, as evidenced by the anticorrelation between the simulated poroelastic interferogram and the InSAR data (Figure 6). The sense of motion in the LOS direction is essentially the same over 6 months and 3 years after the earthquake, as inferred from the corresponding InSAR data (pairs denoted by black lines in Figure 2 and shown in Figure 8). This is indicative of either very small effective fluid diffusivity, or absence of pore fluids in the upper crust in the Chuya Range and basin. This is somewhat surprising, given that poroelastic rebound was previously inferred in quite diverse tectonic environments [*Jónsson et al.*, 2003; *Fialko*, 2004b; *Freed et al.*, 2006]. For example, in areas as arid as the Mojave Desert, the fluid diffusion was proposed to be a dominant contribution of the postseismic transient imaged by InSAR during several years following the Landers earthquake [*Peltzer et al.*, 1998; *Fialko*, 2004b].

[19] The 3 years of postseismic deformation following the Altai earthquake are best explained by shallow slip in the seismogenic zone. One possible interpretation of such slip is that the latter occurs in response to a stress concentration on the periphery of large coseismic slip areas. Accelerated motion on a deep extension of the fault may occur aseismically, representing either velocity strengthening behavior or viscous-like deformation within a localized subvertical shear zone in the middle and lower crust [*Fialko*, 2004b]. Another possibility is that the observed deformation results from stick-slip motion in the brittle layer [*Dieterich*, 1994; *Perfettini and Avouac*, 2007]. Our inversions indicate that the geodetic moment released during 3 years of postseismic transient was $M_0 = 2.32 \times 10^{18}$ N m (assuming a shear modulus of 33 GPa), which is comparable to a cumulative moment of aftershocks derived from long-period body wave and surface wave data, $M_0 = 1.51 \times 10^{18}$ N m [*Ekström et al.*, 2005]. Some of the aftershocks may not have occurred on the 2003 Altai rupture, so the latter estimate should be considered an upper bound. Given the uncertainty ($\sim$0.1°) in the teleseismically recorded event locations, there is permissive, but not conclusive evidence that most of the aftershock activity is concentrated on the fault that produced the main shock. We minimized a potential bias by summing the seismic moment of aftershocks having magnitude 4 and above, 20 km from the epicenter, a distance corresponding to twice the location standard deviation, and verified that the temporal distribution of selected events follows Omori's law. The corresponding aftershocks of magnitude 5 and above are shown in Figure 1. Note that the estimate of the epicenter location was bias by about 20 km so a similar error can be expected for aftershocks. Figure 8 shows the cumulative seismic moment released from 13 October 2003, date of the first available postseismic InSAR data. Interferogram 19 July 2004 to 22 December 200 spans a time interval about three times smaller than interferogram 19 June 2006 to 19 July 2004 yet exhibits comparable

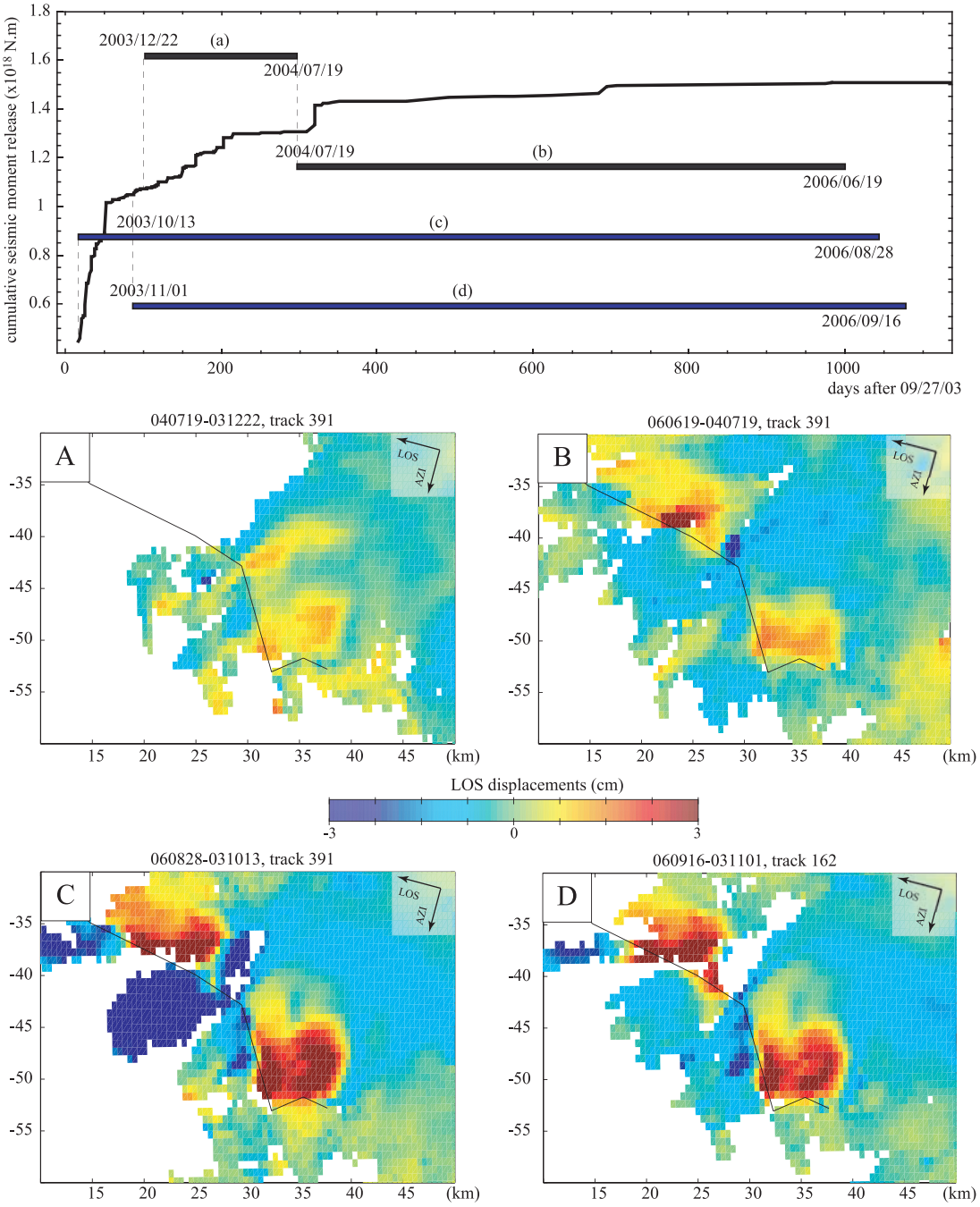

Figure 8. Seismic moment release. Cumulative seismic moment after 13 October 2003 and the LOS displacement of available InSAR data. The LOS displacements correlate with the seismic moment released in the corresponding time interval of each interferometric pair. The thin black line indicates the fault surface location. (a–d) LOS displacements in UTM coordinates relative to the origin (87.74°E, 50.30°N).

LOS displacements. Similarly, a comparable amount of seismic moment was released in the corresponding time intervals. Interferometric pairs 28 August 2006 to 13 October 2003 and 16 September 2006 to 1 November 2003 (Figures 8c and 8d, respectively) cover about the same time interval, but the former records the deformation a month earlier than the latter, and shows greater LOS displacements. The available InSAR data depict a deformation that correlates qualitatively with the time-dependent release of seismic energy of aftershocks. The inferred occurrence of postseismic slip in the seismogenic zone between two areas of high coseismic slip (5c and 4c), along with the general agreement between the teleseismically derived moment of aftershocks and the geodetic moment suggested by our inverse model (5c) indicate that most of the postseismic deformation detected by InSAR my be explained in terms of continued seismic moment release. We cannot rule out a possibility that at least some slip on the fault might have occurred aseismically, but the available observations suggest that aseismic afterslip did not domi-

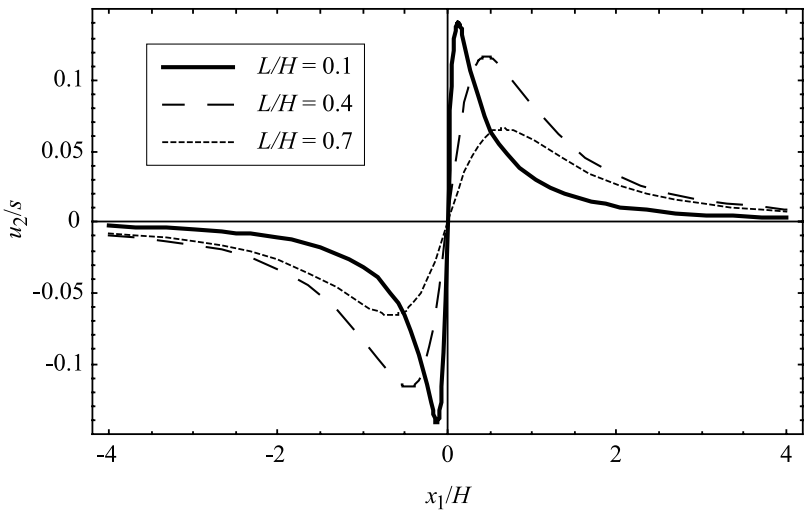

Figure 9. Difference between the full relaxation of the coseismic stresses on a vertical plane (afterslip) and on a horizontal plane (viscoelastic relaxation). In both cases, the seismogenic zone, of thickness H, is perfectly elastic and the fault extends from the surface to a depth L. The two-dimensional solution is self-similar and depends only on the dimensionless parameter $h = L/H$.

nate the postseismic relaxation contrary to inferences from other locations [*Rymer*, 1990; *Savage and Svarc*, 1997; *Jacobs et al.*, 2002; *Hearn et al.*, 2002; *Fialko*, 2004b]. Localized creep in the lower crust and upper mantle is a suggested mechanism for the loading on the fault in the interseismic period [*Savage and Prescott*, 1978], and it is reasonable to expect that coseismic loading would result in an accelerated creep on a deep extension of the fault [*Tse and Rice*, 1986; *Fialko*, 2004b]. However, the deep afterslip is not evident in the 3 year postseismic transient following the Altai earthquake. Our kinematic inversion did not require slip on a downdip extension of the fault. In fact, a relatively short wavelength of the observed deformation transient precludes any contribution from possible relaxation phenomena below the brittle-ductile transition. To quantify this statement, we present analytical solutions for deep afterslip and viscoelastic response in the limit of complete relaxation in two dimensions (antiplane strain). Consider a screw dislocation extending from the surface to a locking depth L. In the presence of a viscoelastic substrate below the depth H, the surface displacement after full relaxation of the coseismic stress change is (see Appendix B)

$$u(x) = \frac{s}{\pi} \tan^{-1}\left(\tan\frac{\pi L}{2H}\coth\frac{\pi x}{2H}\right) \tag{1}$$

where x is the horizontal distance from the fault and s is the total displacement occurring across the fault. In case of afterslip, the stress relaxation is believed to occur on a vertical plane below the seismogenic fault. As shown in Appendix B, such relaxation gives rise to the following displacement at the surface:

$$u(x) = \frac{s}{\pi} \tan^{-1}\left(\frac{H}{x}\sqrt{1+\frac{x^2}{H^2}}\tan\frac{\pi L}{2H}\right) \tag{2}$$

Figure 9 presents a comparison between the surface displacements due to viscoelastic relaxation and deep afterslip. For the same depth of the brittle-ductile transition H, and L/H ratio, the afterslip model produces a more localized deformation compared to the viscoelastic model. However, the wavelength of surface displacements in both cases is of the order of H. This result also holds in three dimensions (the main difference being vanishing of surface displacements in the far field in case of 3-D deformation). InSAR observations of postseismic deformation over 3 years following the Altai earthquake do not reveal lobes of LOS displacements with wavelengths greater than 20 km, indicating that the source is confined to the upper crust. The lack of long-wavelength deformation prevents us from considering more complicated (and presumably, more realistic) models of viscoelastic relaxation using nonlinear rheologies. Therefore we conclude that the bulk of the observed postseismic transient is due to additional slip on the fault plane at the periphery of areas with high coseismic slip. The postseismic fault adjustment is dominated by aftershocks but some aseismic creep in the upper crust cannot be ruled out.

5. Conclusions

[20] The 27 September 2003, M_w7.2 right-lateral strike-slip Altai earthquake ruptured a subvertical fault from the surface to a depth of ~12 km, as inferred from a kinematic inversion of SAR interferograms from the adjacent satellite tracks. Our InSAR observations do not have the spatial coverage to constrain the mantle viscosity at depths greater than about 40 km. We can, however, put a lower bound on the dynamic viscosity of the lower crust of 10^{19} Pa s. A smaller viscosity would have caused a substantial surface deformation detectable by the InSAR data. The postseismic deformation, as observed from all interferograms covering a time interval up to 3 years, cannot be explained by the viscous relaxation of any horizontal substrate above 35 km depth. The polarity of the postseismic displacements around the fault does not warrant the poroelastic rebound in the upper crust, suggesting a very low permeability or fluid saturation of the crustal rocks in the Chuya depression and

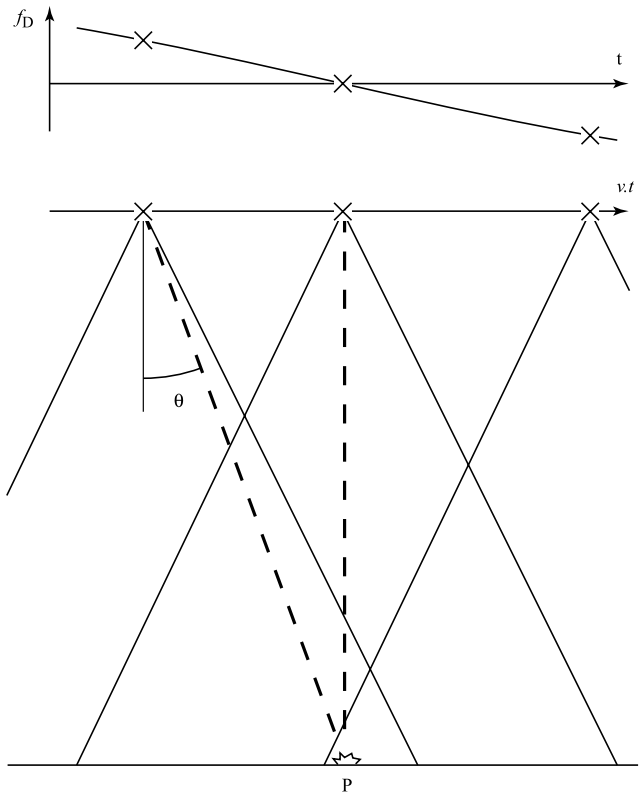

Figure A1. Doppler history f_D as a function of time, or equivalently, as a function of the look direction toward a scatterer P at the surface of the Earth. Positive and negative Doppler frequencies are associated with positive and negative look directions, respectively.

Chuya Range. We cannot rule out, however, a possibility of a rapid pore fluid flow within the first 16 d following the earthquake, an interval for which we have no constraints from interferometry. According to our afterslip model obtained from a joint kinematic inversion of 2 independent interferograms, the total seismic moment release during the 3 years of the postseismic transient was $M_0 = 2.32 \times 10^{18}$ N m. This estimate has the same order of magnitude as the cumulative aftershock moment of $M_0 = 1.51 \times 10^{18}$ N m derived from long-period body wave and surface wave data over the corresponding time interval. Most of the 3 year line-of-sight displacements can be explained by the occurrence of aftershocks in the brittle upper crust next to areas of high coseismic slip. Some slip may have occurred aseismically at depths less than 6 km. These results differ from those from other areas, and may be indicative of variations in rheology of the continental lithosphere in different tectonically active areas.

Appendix A

A1. Along-Track Interferometry

[21] Conventional SAR interferometry allows one to measure surface displacements along the satellite line of sight (radar range). Any component of motion that is orthogonal to the LOS (for example, the along-track or azimuth displacements) cannot be detected with conventional interferometry. Other techniques utilizing radar amplitude information (e.g., pixel tracking) were proposed to measure azimuthal offsets [*Michel et al.*, 1999; *Van Puymbroeck et al.*, 2000; *Leprince et al.*, 2007; *Fialko et al.*, 2001]. Such techniques involve subpixel correlation of the radar images, and are computationally expensive. Recently, [*Bechor and Zebker*, 2006] presented a new way to measure along-track displacements by forming forward looking and backward looking interferograms and computing their phase difference. The resulting image is a measure of the surface displacement projected in the azimuthal direction and the LOS plane. We propose a different way of generating the along-track interferogram by utilizing the already focused SAR images. Our method consists in filtering for positive and negative Doppler frequencies of the full resolution complex SAR images. The proposed method is computationally efficient and can be easily implemented in existing SAR processors.

[22] The high resolution of SAR imagery is obtained via bandwidth broadening. In the range direction, this is achieved by pulse compression. Along track, resolution is improved by making use of a Doppler synthesis or synthetic array approach [e.g., *Elachi*, 1987]. In the along-track, or azimuthal direction, the SAR geometry implies several relationships between time, frequency, velocity, look angle and satellite position. For instance, the instantaneous look angle θ, between the radar antenna and a scatterer, and the Doppler frequency f_D are related as follows:

$$f_D = \frac{2v}{\lambda} \sin\theta \tag{A1}$$

where λ is the radar wavelength and v is the platform velocity (Figure A1). This relation allows one to select look angles by using the frequency content of the radar return. As the SAR image lines are recorded at the frequency f_{PRF}, the local look angle is also a function of time, and equation (A1) allows one to evaluate the radiation pattern of the SAR antenna as a function of time. In order to build forward looking and backward looking interferograms, we only need to separate the positive and negative Doppler returns. Because of the Earth's rotation and curvature and the platform's yaw, the zero Doppler f_0 does not exactly have a zero azimuth frequency, and is a function of range r. Energy distributed above the Doppler centroid corresponds to forward looking angles and energy associated with frequencies lower than f_0 corresponds to the backward looking part of the antenna beam. Our method thus consists in taking the one-dimensional Fourier transform in the azimuthal direction of each single look complex image and either tapering to zero unwanted frequencies or simply cropping the spectrum in order to select returns with a given Doppler sign. We do so for two SAR complex images, and we obtain 4 complex subimages. We denote a_{11}, a_{12} the forward looking and backward looking parts of image 1, respectively; and a_{21}, a_{22} the corresponding parts of image 2. Thus

$$\begin{aligned} \phi_1 &= \arg\left(a_{11}\, a_{21}^*\right) \\ \phi_2 &= \arg\left(a_{12}\, a_{22}^*\right) \end{aligned} \tag{A2}$$

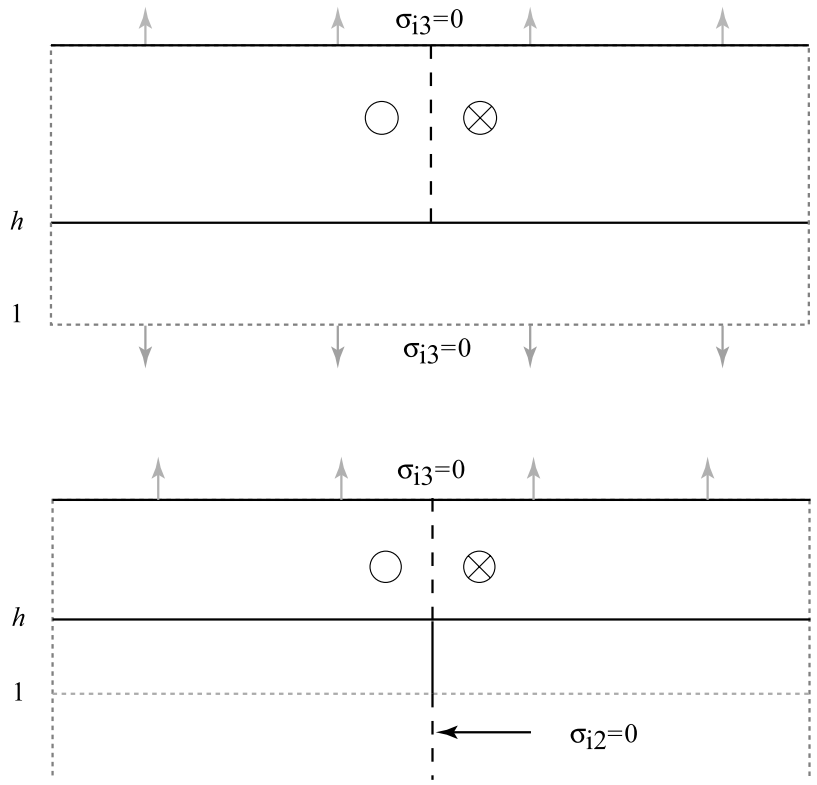

Figure A2. Geometry and boundary conditions applied to the screw dislocation in an elastic half-space. The solutions represent the sum of the coseismic and postseismic contributions to the antiplane displacement. (top) Free surface on a horizontal plane corresponding to the viscoelastic relaxation. (bottom) Free surface on a downdip extension of the fault plane corresponding to the afterslip scenario.

are the phase of the forward and backward interferograms, respectively. The along-track interferogram is the conjugate product $a_{11}\, a^*_{21} a^*_{12}\, a_{22}$. We now consider a scatterer in the LOS plane that moved $\Delta\mathbf{r}$ between the two acquisitions while staying in the LOS plane. The pulse energy is distributed along different angles so we call α the average look angle of half the beam aperture. Exploiting the parallax effect between the forward and backward look angles, and making use of simple trigonometric relations, the phase of the along-track interferogram is

$$\Delta\phi = \frac{8\pi}{\lambda} \sin\alpha\, \Delta\mathbf{r} \cdot \hat{\mathbf{a}} \tag{A3}$$

where $\hat{\mathbf{a}}$ is a unit vector in the orbit direction and in the LOS plane. This is a measure of the azimuthal component of the displacement. The averaged look angle, assuming a non-tapered rectangular aperture, is

$$\alpha = \frac{\lambda}{L} \frac{\int_0^1 \theta\, \mathrm{sinc}^2\theta\, d\theta}{\int_0^1 \mathrm{sinc}^2\theta\, d\theta} \approx \frac{\lambda}{3.65\, L} \tag{A4}$$

where L is the antenna length and the sinc function is the theoretical angular distribution of the radar amplitude. In practice, the emitted pulse is tapered to avoid aliasing, which slightly changes the radiation pattern. (If the angular distribution were uniform, one would have $\alpha = \lambda/2L$.) In order to simplify the discussion, we make the conservative approximation $\alpha = \lambda/4L$. Noting that $\alpha \ll 1$, we can write

$$\Delta\phi = 2\pi \frac{\Delta\mathbf{r} \cdot \hat{\mathbf{a}}}{L} \tag{A5}$$

The phase measurement is independent of the radar wavelength and is only a function of the radar antenna length and the horizontal component of the ground displacement. Furthermore, as L is about 10 m, relatively large displacements, of the order of 0.1–1 m, are needed to generate acceptable signal-to-noise ratio. Because of the double phase difference, the along-track phase measurement is not relative, as opposed to conventional interferometry. A phase jump should occur at $\Delta\mathbf{r} \cdot \hat{\mathbf{a}} = L/2$, but the coherence is lost when displacements $\Delta\mathbf{r} \cdot \hat{\mathbf{a}}$ are greater than $L/4$, half the pixel size in the azimuth direction. Therefore the obtained phase signal does not have the usual properties: it is not relative and phase jumps occur because of speckle only, not because of ground displacements. There is no need for phase unwrapping to uncover the azimuthal displacement field and the measured displacement lies in the range $[-L/4, L/4]$.

A2. Full Relaxation Due to a Screw Dislocation

[23] We consider a full relaxation at a depth H below an infinitely long screw dislocation extending from the surface to a depth L, with an antiplane slip s (Figure A2). The displacement field is self-similar, so we introduce the dimensionless parameters $x_1 = x_1^*/H$, $x_3 = x_3^*/H$ and $h =$

L/H, where the starred variables are the dimensional Cartesian coordinates. The corresponding surface displacements can be expressed using the general solution for an antiplane dislocation in a layered half plane of *Weertman and Weertman* [1964] and *Rybicki* [1971] by setting to zero the shear modulus of the underlying half-space (first line in equation (A6)). This solution is in the form of an infinite series, and converges rather slowly. One way to improve convergence is to compute the series dual through Poisson's sum formula (second line in equation (A6)). The solution is still in the form of an infinite series. As the antiplane screw dislocation problem consists essentially in solving Laplace's equation, a simplification comes from conformal mapping. Indeed, by the application of the mapping $w = \ln\frac{z-1}{z+1}$, we notice that the coseismic screw dislocation in a plate, corresponding to the viscoelastic full relaxation, is the dual of the interseismic dislocation in a half-space. The equivalent solutions are

$$\begin{aligned} u_2(x_1) &= \frac{2}{\pi}\left[\tan^{-1}\frac{h}{x_1} + \sum_{k=1}^{\infty}\tan^{-1}\frac{h-2k}{x_1} + \tan^{-1}\frac{h+2k}{x_1}\right] \\ &= h + 2\sum_{k=1}^{\infty}\frac{\sin k\pi h}{k\pi}\, e^{-k\pi x_1} \\ &= \frac{2}{\pi}\tan^{-1}\frac{\tan \pi h/2}{\tanh \pi x_1/2} \end{aligned} \tag{A6}$$

The solution for afterslip, with a vertical stress-free surface extending from the dimensionless depth $x_3 = 1$ to infinity (bottom of Figure A2), can be also obtained with the help of conformal mapping: the afterslip and the plate solutions are dual through the mapping $w = \sin z$. It can be readily shown that the solution for afterslip in the limit of full relaxation is

$$\begin{aligned} u_2(x_1, 0) &= h + 2\sum_{k=1}^{\infty}\frac{\sin k\pi h}{k\pi}\, e^{-2k\,\mathrm{asinh} x_1} \\ &= \frac{2}{\pi}\tan^{-1}\left(\frac{1}{x_1}\sqrt{1+x_1^2}\,\tan\frac{\pi}{2}h\right) \end{aligned} \tag{A7}$$

The difference between the surface displacement due to the antiplane dislocation in a plate and the dislocation underlain by a vertical stress-free surface shows how these end-member models result in different spatial wavelengths of postseismic deformation at the surface.

[24] **Acknowledgments.** We thank Rowena Lohman, an anonymous reviewer, and the Associate Editor for their thorough and thoughtful reviews of this manuscript. We acknowledge E. Nissen for providing us with his mapping of the surface rupture in digital format. This work was supported by NSF (grant EAR-0450035) and SCEC. Original SAR data were provided by the European Space Agency. Numerical codes used in this study are available from the authors.

References

Bayasgalan, A., J. Jackson, and D. McKenzie (2005), Lithosphere rheology and active tectonics in Mongolia: Relations between earthquake source parameters, gravity and GPS measurements, *Geophys. J. Int.*, *163*, 1151–1179.

Bechor, N. B. D., and H. A. Zebker (2006), Measuring two-dimensional movements using a single InSAR pair, *Geophys. Res. Lett.*, *33*, L16311, doi:10.1029/2006GL026883.

Biot, M. A. (1941), General theory of three-dimensional consolidation, *Appl. Phys.*, *12*, 155–164.

Brace, W. F., and D. L. Kohlstedt (1980), Limits on lithospheric stress imposed by laboratory experiments, *J. Geophys. Res.*, *85*, 6248–6252.

Calais, E., M. Vergnolle, V. San'kov, A. Lukhnev, A. Miroshnitchenko, S. Amarjargal, and J. Déverchère (2003), GPS measurements of crustal deformation in the Baikal-Mongolia area (1994–2002): Implications for current kinematics of Asia, *J. Geophys. Res.*, *108*(B10), 2501, doi:10.1029/2002JB002373.

Coussy, O. (2004), *Poromechanics*, John Wiley, Chichester, U.K.

Cunningham, D. (2005), Active intracontinental transpressional mountain building in the Mongolian Altai: Defining a new class of orogen, *Earth Planet. Sci. Lett.*, *240*, 436–444.

Cunningham, W. D. (1998), Lithospheric controls on late Cenozoic construction of the Mongolian Altai, *Tectonics*, *17*, 891–902.

Deng, J., K. Hudnut, M. Gurnis, and E. Hauksson (1999), Stress loading from viscous flow in the lower crust and triggering of aftershocks following the 1994 Northridge, California, earthquake, *Geophys. Res. Lett.*, *26*, 3209–3212.

Dieterich, J. (1994), A constitutive law for rate of earthquake production and its application to earthquake clustering, *J. Geophys. Res.*, *99*, 2601–2618.

Dieterich, J. H. (1987), Nucleation and triggering of earthquake slip: Effect of periodic stresses, *Tectonophysics*, *144*, 127–139.

Ekström, G., A. M. Dziewoński, N. N. Maternovskaya, and M. Nettles (2005), Global seismicity of 2003: Centroid moment-tensor solutions for 1087 earthquakes, *Phys. Earth Planet. Inter.*, *148*, 251–327.

Elachi, C. (1987), *Spaceborne Radar Remote Sensing: Applications and Techniques*, IEEE Press, New York.

Fialko, Y. (2004a), Probing the mechanical properties of seismically active crust with space geodesy: Study of the coseismic deformation due to the 1992 M_w 7.3 Landers (southern California) earthquake, *J. Geophys. Res.*, *109*, B03307, doi:10.1029/2003JB002756.

Fialko, Y. (2004b), Evidence of fluid-filled upper crust from observations of postseismic deformation due to the 1992 M_w7.3 Landers earthquake, *J. Geophys. Res.*, *109*, B08401, doi:10.1029/2004JB002985.

Fialko, Y., M. Simons, and D. Agnew (2001), The complete (3-D) surface displacement field in the epicentral area of the 1999 M_w 7.1 Hector Mine earthquake, California, from space geodetic observations, *Geophys. Res. Lett.*, *28*, 3063–3066.

Fialko, Y., D. Sandwell, M. Simons, and P. Rosen (2005), Three-dimensional deformation caused by the Bam, Iran, earthquake and the origin of shallow slip deficit, *Nature*, *435*, 295–299.

Freed, A. M., and R. Bürgmann (2004), Evidenve of power-law flow in the Mojave desert mantle, *Nature*, *430*, 548–551.

Freed, A. M., R. Bürgmann, E. Calais, J. Freymueller, and S. Hreinsdttir (2006), Implications of deformation following the 2002 Denali, Alaska, earthquake for postseismic relaxation processes and lithospheric rheology, *J. Geophys. Res.*, *111*, B01401, doi:10.1029/2005JB003894.

Gasperini, P., G. D. Forno, and E. Boschi (2004), Linear or non-linear rheology in the Earth's mantle: The prevalence of power-law creep in the postglacial isostatic readjustment of Laurentia, *Geophys. J. Int.*, *157*, 1297–1302.

Hamiel, Y., and Y. Fialko (2007), Structure and mechanical properties of faults in the North Anatolian Fault system from InSAR observations of coseismic deformation due to the 1999 Izmit (Turkey) earthquake, *J. Geophys. Res.*, *112*, B07412, doi:10.1029/2006JB004777.

Hearn, E. H., R. Bürgmann, and R. E. Reilinger (2002), Dynamics of Izmit earthquake postseismic deformation and loading of the Düzce earthquake hypocenter, *Bull. Seismol. Soc. Am.*, *92*, 172–193.

Jacobs, A., D. Sandwell, Y. Fialko, and L. Sichoix (2002), The 1999 (M_w 7.1) Hector Mine, California, earthquake: Near-field postseismic deformation for ERS interferometry, *Bull. Seismol. Soc. Am.*, *92*, 1433–1442.

Jónsson, S., P. Segall, R. Pederson, and G. Björnsson (2003), Post-earthquake ground movements correlated to pore-pressure transients, *Nature*, *424*, 179–183.

Karato, S., and P. Wu (1993), Rheology of the upper mantle: A synthesis, *Science*, *260*, 771–778.

Kenner, S. J., and P. Segall (2000), Postseismic deformation following the 1906 San Francisco earthquake, *J. Geophys. Res.*, *105*, 13,195–13,210.

Larsen, T. B., D. A. Yuen, A. V. Malevsky, and J. L. Smedsmo (1996), Dynamics of strongly time-dependent convection with non-Newtonian temperature-dependent viscosity, *Phys. Earth Planet. Inter.*, *94*, 75–103.

Leprince, S., S. Barbot, F. Ayoub, and J. P. Avouac (2007), Automatic, precise, ortho-rectification and coregistration for satellite image correlation, application to ground deformation measurement, *IEEE Trans. Geosci. Remote Sens.*, *45*, 1529–1558.

Massonnet, D., M. Rossi, C. Carmona, F. Adragna, G. Peltzer, K. Feigi, and T. Rabaute (1993), The displacement field of the landers earthquake mapped by radar interferometry, *Nature*, *364*, 138–142.

Michel, R., J.-P. Avouac, and J. Taboury (1999), Measuring ground displacements from SAR amplitude images: Application to the Landers earthquake, *Geophys. Res. Lett.*, *26*, 875–878.

Nissen, E., B. Emmerson, G. J. Funning, A. Mistrukov, B. Parsons, D. P. Robinson, E. Rogozhin, and T. J. Wright (2007), Combining inSAR and

seismology to study the 2003 Siberian Altai earthquakes-dextral strike-slip and anticlockwise rotations in the northern India-Eurasia collision zone, *Geophys. J. Int.*, *169*, 216–232.

Nur, A., and G. Mavko (1974), Postseismic viscoelastic rebound, *Science*, *183*, 204–206.

Okada, Y. (1985), Surface deformation due to shear and tensile faults in a half-space, *Bull. Seismol. Soc. Am.*, *75*, 1135–1154.

Peltier, W. R. (1981), Ice age geodynamics, *Annu. Rev. Earth Planet. Sci.*, *9*, 199–225.

Peltzer, G., P. Rosen, F. Rogez, and K. Hudnut (1998), Poroelastic rebound along the Landers 1992 earthquake surface rupture, *J. Geophys. Res.*, *103*, 30,131–30,145.

Peltzer, G., F. Campé, and G. King (1999), Evidence of nonlinear elasticity of the crust from the M_w7.6 Manyi (Tibet) earthquake, *Science*, *286*, 272–275.

Perfettini, H., and J.-P. Avouac (2004), Postseismic relaxation driven by brittle creep: A possible mechanism to reconcile geodetic measurements and the decay rate of aftershocks, application to the Chi-Chi earthquake, Taiwan, *J. Geophys. Res.*, *109*, B02304, doi:10.1029/2003JB002488.

Perfettini, H., and J.-P. Avouac (2007), Modeling afterslip and aftershocks following the 1992 Landers earthquake, *J. Geophys. Res.*, *112*, B07409, doi:10.1029/2006JB004399.

Piombo, A., G. Martinelli, and M. Dragoni (2005), Post-seismic fluid flow and coulomb stress changes in a poroelastic medium, *Geophys. J. Int.*, *162*, 507–515.

Pollitz, F. F. (1997), Gravitational viscoelastic postseismic relaxation on a layered spherical Earth, *J. Geophys. Res.*, *102*, 17,921–17,942.

Pollitz, F. F. (2003), Transient rheology of the uppermost mantle beneath the Mojave desert, California, *Earth Planet. Sci. Lett.*, *215*, 89–104.

Pollitz, F. F., G. Peltzer, and R. Bürgmann (2000), Mobility of continental mantle: Evidence from postseismic geodetic observations following the 1992 Landers earthquake, *J. Geophys. Res.*, *105*, 8035–8054.

Reid, H. F. (1910), *The California Earthquake of April 18, 1906, vol. 2, The Mechanics of the Earthquake*, Carnegie Inst. of Washington, Washington, D. C.

Reilinger, R. (1986), Evidence for postseismic viscoelastic relaxation following the 1959 M = 7.5 Hebgen Lake, Montana, earthquake, *J. Geophys. Res.*, *91*, 9488–9494.

Rosen, P. A., S. Hensley, I. R. Joughin, F. K. Li, S. N. Madsen, E. Rodriguez, and R. M. Goldstein (2000), Synthetic aperture radar interferometry, *Proc. IEEE*, *80*, 333–382.

Rybicki, K. (1971), The elastic residual field of a very long strike-slip fault in the presence of a discontinuity, *Bull. Seismol. Soc. Am.*, *61*, 79–92.

Rymer, M. J. (1990), Near-fault meaurement of postseismic slip associated with the 1989 Loma Prieta, California, earthquake, *Geophys. Res. Lett.*, *17*, 1789–1792.

Savage, J. C., and W. H. Prescott (1978), Asthenosphere readjustement and the earthquake cycle, *J. Geophys. Res.*, *83*, 3369–3376.

Savage, J. C., and J. L. Svarc (1997), Postseismic deformation associated with the 1992 M_w = 7.3 Landers earthquake, southern California, *J. Geophys. Res.*, *102*, 7565–7578.

Savage, J. C., M. Lisowski, and J. L. Svarc (1994), Postseismic deformation following the 1989 (M = 7.1) Loma Prieta, California, earthquake, *J. Geophys. Res.*, *99*, 13,757–13,765.

Simons, M., Y. Fialko, and L. Rivera (2002), Coseismic deformation from the 1999 M_w 7.1 Hector Mine, California, earthquake as inferred from InSAR and GPS observations, *Bull. Seismol. Soc. Am.*, *92*, 1390–1402.

Stein, R. S., and M. Lisowski (1983), The 1979 Homestead Valley earthquake sequence, California: Control of aftershocks and postseismic deformation, *Geophys. Res.*, *88*, 6477–6490.

Tapponier, P., and P. Molnar (1979), Active faulting and Cenozoic tectonics of the Tien Shan, Mongolia, and Baykal regions, *J. Geophys. Res.*, *84*, 3425–3459.

Tarayre, H., and D. Massonnet (1996), Atmospheric propagation heterogeneities revealed by ERS-1 interferometry, *Geophys. Res. Lett.*, *23*, 989–992.

Thatcher, W. (1983), Nonlinear strain buildup and the earthquake cycle on the San Andreas fault, *J. Geophys. Res.*, *88*, 5893–5902.

Thatcher, W., and J. R. Rundle (1979), A model for the earthquake cycle in underthrust zones, *J. Geophys. Res.*, *84*, 5540–5556.

Tse, S. T., and J. R. Rice (1986), Crustal earthquake instability in relation to the depth variation of frictional slip properties, *J. Geophys. Res.*, *91*, 9452–9472.

Van Puymbroeck, N., R. Michel, R. Binet, J.-P. Avouac, and J. Taboury (2000), Measuring earthquakes from optical satellite images, *Appl. Opt.*, *39*, 3486–3494.

Wang, R., F. L. Martin, and F. Roth (2003), Computation of deformation induced by earthquakes and a multi-layered elastic crut—FORTRAN programs EDGRN/EDCMP, *Comput. Geosci.*, *29*, 195–207.

Wang, R., F. Lorenzo-Martin, and F. Roth (2006), PSGRN/PSCMP-a new code for calculating co- and post-seismic deformation, geoid and gravity changes based on the viscoelastic-gravitational dislocation theory, *Comput. Geosci.*, *32*, 527–541.

Weertman, J., and J. Weertman (1964), *Elementary Dislocation Theory*, Macmillan, New York.

Windley, B. F., and M. B. Allen (1993), Mongolian plateau: Evidence for a late Cenozoic mantle plume under central Asia, *Geology*, *21*, 295–298.

Zebker, H. A., and J. Villasenor (1992), Decorrelation in interferometric radarechoes, *Geosci. Remote Sens. Lett.*, *30*, 950–959.

Zhu, L., and L. Rivera (2002), A note on the dynamic and static displacements from a point source in multilayered media, *Geophys. J. Int.*, *148*, 619–627.

S. Barbot and Y. Fialko, Institute of Geophysics and Planetary Physics, Scripps Institution of Oceanography, University of California, San Diego, La Jolla, CA 92093-0225, USA. (sbarbot@ucsd.edu)

Y. Hamiel, Geological Survey of Israel, 30 Malkhei Israel St., Jerusalem 95501, Israel.